Supporting Information

Net landscape carbon balance of a tropical savanna: relative importance of fire and aquatic export in offsetting terrestrial production

Clément Duvert, Lindsay B. Hutley, Jason Beringer, Michael I. Bird, Christian Birkel, Damien T. Maher, Matthew Northwood, Mitchel Rudge, Samantha A. Setterfield, Jonathan G. Wynn

Contents of this file

Methods S1. DOC flux calculations

We used an S-can spectro::lyser (Messtechnik GmbH) for in situ, bi-hourly measurements of DOC. This instrument is a portable ultraviolet-visible spectrometer that measures light attenuation between 200 nm and 750 nm (Langergraber *et al.* 2003). DOC is calculated via an internal algorithm using absorption in the range 230-450 nm. The instrument automatically corrects for turbidity effects (measured at 450-650 nm), so that post-hoc correction of DOC values as in Saraceno *et al.* (2017) was not required.

In total, we recorded 2760 optical measurements, corresponding to 32% of coverage over the two years of study – and, critically, 74% of coverage during the more dynamic wet season (January–May). The longest gaps in the time series were during the dry season, when DOC was less variable. In these instances, we gap-filled the series with measurements obtained from grab sampling. Data gaps were due to a variety of issues such as saturation of the sensor, pump failure, and last but not least theft of solar panels.

The optical measurements of DOC were then calibrated using 23 grab samples collected under a wide range of flow conditions. To satisfy the assumption of normality, we log-transformed the optical measurements and 'true' DOC concentrations and derived a type-2 linear regression (MATLAB function *lsqfitma*) between them (Figure S1). The least square fitting using *lsqfitma* is adjusted by minimising both x- and y-residuals.
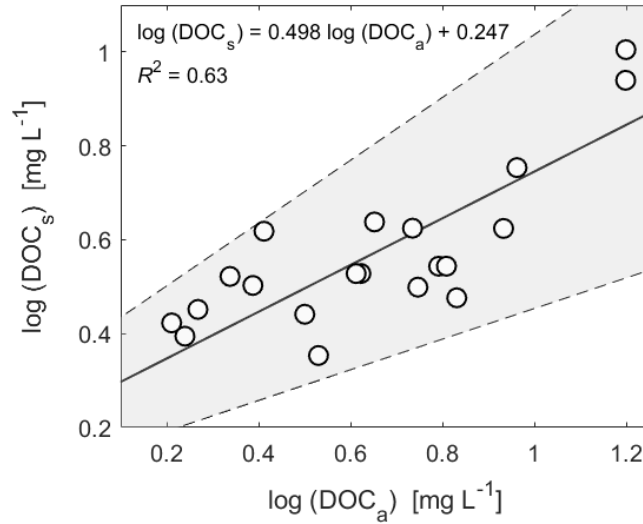
Figure S1. Linear regression (solid line) between log-transformed automated DOC measurements (log (DOC$_a$)) and log-transformed sample DOC concentrations (log (DOC$_s$)) in the Howard River. The dashed lines and grey shaded area correspond to the 99% confidence intervals of the regression, which we used in the quantification of uncertainties.

Using the relationship between *in situ* sensor measurements and DOC concentrations, we derived bi-hourly time-series of calibrated DOC (Figure S2). All gaps in the series were filled with (i) manual measurements and (ii) linear interpolation between existing values.
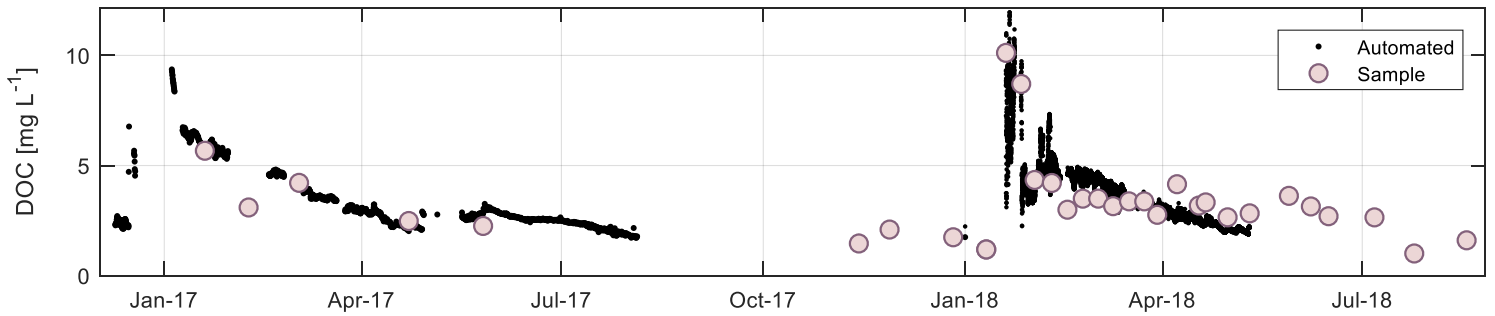
Figure S2. Calibrated automated data (black dots) and DOC concentrations from grab samples (purple circles) in the Howard River.

Methods S2. DIC flux calculations

In total, we recorded 5606 *in situ* measurements of pCO$_2$, pH and temperature, which we converted into estimates of DIC concentrations using a temperature-dependent approximation of the CO$_2$ solubility constant K_{CO2} (Plummer and Busenberg 1982):

$$\log K_{CO_2} = 108.3865 + 0.01985076\,T - \frac{6919.53}{T} - 40.4515 \log T + \frac{669365}{T^2},$$

and the carbonate dissociation constants (Harned and Davis 1943):

$$PK_1 = \frac{3404.71}{T} + 0.032786\,T - 14.8435$$

$$PK_2 = \frac{2902.39}{T} + 0.02379\,T - 6.498$$

The obtained DIC data cover 64% of the two years of study, with most data gaps during the low flow periods. In these instances, we gap-filled the series with measurements obtained from grab sampling.

The DIC values based on *in situ* measurements were then calibrated using 17 grab samples collected under a wide range of flow conditions. We used a type-2 linear regression (MATLAB function *lsqfitma*) between automated measurements and 'true' DIC concentrations (Figure S3):
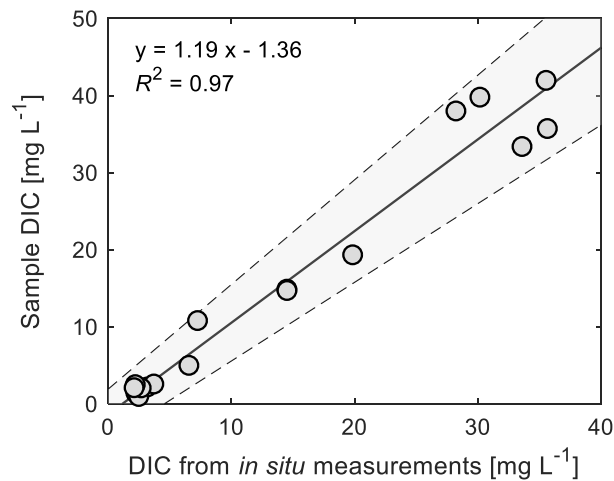
Figure S3. Linear regression (solid line) between DIC estimates based on automated pCO₂, pH and temperature (*x*) and measured DIC concentrations (*y*) in the Howard River. The dashed lines and grey shaded area correspond to the 99% confidence intervals of the regression, which we used in the quantification of uncertainties.

Using the relationship between *in situ* estimates and DIC concentrations, we derived bi-hourly time-series of calibrated DIC (Figure S4). All gaps in the series were filled with (i) manual measurements and (ii) linear interpolation between existing values.
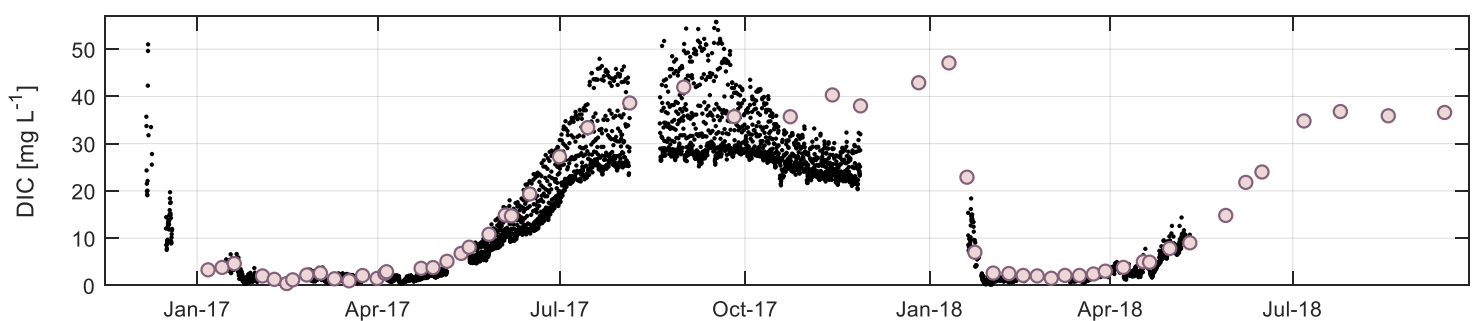
Figure S4. Calibrated automated DIC data (black dots) and DIC concentrations from grab samples (purple circles) in the Howard River.

Note that the large variability in DIC concentrations during the July-17 to October-17 period corresponds to greater amplitude in diurnal DIC cycles. This is related to higher water residence times and increased importance of river metabolism during the dry season. The observed diurnal cycles did not result in significant changes in the annual DIC load, as these values corresponded to low flow conditions.

Methods S3. Quantification of uncertainties on DIC and DOC load estimates

Uncertainties on the total DOC and DIC load estimates were assessed through a Monte Carlo error propagation approach following the below workflow:

1) For each bi-hourly timestep, we generated 10,000 sets of discharge values and 10,000 sets of concentration values – for discharge, we used a Gaussian distribution centred on the measured value and with relative standard deviation ±20% of the measured value, while for C concentrations, we used a beta distribution (α=3; β=3) bounded by the 99% prediction interval as given by the calibration curves (Figures S1 and S3). This beta distribution is in many ways similar to a truncated Gaussian distribution.

2) From the sets of values generated in 1), we randomly sampled 10,000 multiplication pairs of discharge and concentration values for each timestep and derived 10,000 flux estimates. We then extracted an error range for each timestep as defined by the interval between percentiles 2.5 and 97.5 ($P_{97.5} - P_{2.5}$), roughly equivalent to ±2σ.

3) Total annual loads were obtained by summing up the bi-hourly flux estimates obtained in 2). We thereby obtained 10,000 estimates of total load, from which we extracted the median. Because independent errors tend to cancel out, calculating the error based on these 10,000 load estimates would yield artificially small uncertainties (e.g. Horgby *et al.* 2019). We therefore opted for a more conservative approach, where the uncertainty on total loads ΔL ($\approx$±2σ) was obtained from the root sum of squared errors on flux estimates at each timestep *t*:

$$\Delta L = 2 \times \sqrt{\Sigma_t \left(P_{97.5_t} - P_{2.5_t}\right)^2}$$

Doing this we assumed no autocorrelation of the data, which has been a common assumption in recent studies (e.g. Boix Canadell *et al.* 2019).

Methods S4. POC flux calculations

Unlike for DIC and DOC, the annual POC load was estimated based on manual measurements only. We collected 13 one-litre samples in 2018 under different flow conditions, which we used to quantify POC concentrations. We first filtered a known volume of each sample using pre-weighed glass microfibre filters (Whatman GF/F 0.7µm). Filters were then dried for 2h at 105°C and reweighed to determine total suspended solid concentrations. After drying, filters were immediately stored in sterile 2 mL Eppendorf tubes and kept at -20°C until they were sent for POC analysis. Filters were later analysed at Southern Cross University on a Flash elemental analyser and a Delta V Plus isotope ratio mass spectrometer (Thermo Scientific), as per the procedure described in Maher *et al.* (2013).

Because our POC dataset was limited in size, we were not able to directly derive POC fluxes from the discharge and concentration series. We used the LOAD ESTimator (LOADEST) software package (Runkel *et al.* 2004), particularly adapted for the estimation of constituent loads when flow data are available but matched by irregular concentration measurements.

We chose the Adjusted Maximum Likelihood Estimation method to optimise the calibration and estimation procedures within LOADEST. The program builds a total of nine predictive models, and we used Akaike's Information Criterion to select the best fit:

$$\ln F_{POC} = 4.3729 + 1.4086 \ln Q + 0.8133 \sin 2\pi t - 0.5518 \cos 2\pi t$$

where F_{POC} is the daily POC load, Q is the mean daily discharge, and t is the centred decimal time. We report uncertainties on the total POC load estimate as provided by LOADEST, i.e. the 95% confidence interval ($\approx\pm2\sigma$) on the predicted annual load.

Methods S5. CO_2 evasion

The rate of CO_2 evasion from the river network was estimated using three independent methods. Rather than estimates based on chamber measurements, which can be difficult to undertake under flooded conditions and may not necessarily be representative of the whole stream network, we opted for a mass balance approach (method 1), an estimate based on groundwater recharge calculations (method 2), and the use of common empirical gas exchange models (method 3).

Method 1. Mass balance

This method is based on an earlier characterisation and quantification of different water sources entering the river (Duvert *et al.* 2020). The rate of CO_2 evasion was calculated as the sum of CO_2 losses from each water source to the river outlet. This method resembles that in Hutchins *et al.* (2020), although here we assumed a mixture of several water sources contributing to streamflow. We integrated the mass balance over time such as:

$$F_{CO_2} = \frac{\sum_t \alpha Q_t \left(\overline{C_{\text{shallow gw}}} - C_{\text{river}_t}\right) + \beta Q_t \left(\overline{C_{\text{wetland}}} - C_{\text{river}_t}\right) + \gamma Q_t \left(\overline{C_{\text{deep gw}}} - C_{\text{river}_t}\right)}{A}$$

Where F_{CO2} is the cumulative flux of CO_2 for the study period; Q_t and $C_{\text{river t}}$ are the bi-hourly time series of discharge and CO_2 concentration in the river; $\overline{C_{\text{shallow gw}}}$, $\overline{C_{\text{wetland}}}$ and $\overline{C_{\text{deep gw}}}$ are the average CO_2 concentrations in the three previously identified water sources i.e. shallow groundwater, wetlands and deep groundwater (Duvert et al. 2020); α, β and γ are the relative flow proportions contributed by each source, as defined by Duvert *et al.* (2020) using electrical conductivity and $\delta^{18}O$ as tracers; and A is the catchment area.

Uncertainties related to Method 1 were quantified by generating, for each of the three sources and at each timestep, 10,000 sets of CO_2 concentrations centred on the median and bounded by two standard deviations of the measured concentrations as per Duvert *et al.* (2020). We also generated 10,000 river pCO$_2$ values for each timestep from a Gaussian distribution centred on the measured value and with relative standard deviation $\pm10\%$, as well as 10,000 values of α, β and γ centred on the seasonal estimate given by Duvert *et al.* (2020) and with relative standard deviation $\pm15\%$. We then randomly derived 10,000 evasion estimates for each timestep and extracted the median as well as an error range ($P_{97.5} - P_{2.5}$). As we did for the dissolved load estimates, the uncertainty on total evasion flux was obtained from the root sum of squared errors on flux estimates at each timestep.

Method 2. Groundwater recharge

The second method quantified the flux of DIC recharging the shallow aquifer during the wet season and used this recharge flux as a proxy for DIC export from the terrestrial pool. To do this, we used the water table fluctuation (WTF) method (Healy and Cook 2002) and groundwater level data taken from a monitoring bore intersecting the shallow aquifer (NTG bore RN009421). The method involved first computing a master recession curve, as in Delin *et al.* (2007):

$$H_t = \exp\left(\log\left(H_0 - d\right) + Re \times t\right) + d$$

Where H_0 and H_t are the groundwater levels at the start and end of the recession, respectively, t is time, and d and Re are the two parameters of the regression. We adjusted the master recession curve based on H_0, H_t and t data from eight years (2010–2012; 2014–2018; R^2=0.90; p<0.0001). This master recession curve was then extrapolated to each recession stage of the groundwater level series (Figure S5), so that we could derive, for each year, the height difference between the peak of the rise and extrapolated antecedent recession curve at the time of the peak (ΔH; Figure S5). Estimates of ΔH for 2017 and 2018 were then used to derive recharge rates for these two years as per the WTF method (Healy and Cook 2002):

$$R_T = Sy \times \Delta H_T$$

Where R_T is recharge for year T (mm yr^{-1}), ΔH_T is the groundwater level rise created by recharge for year T (mm), and Sy is the specific yield of the shallow aquifer (unitless).
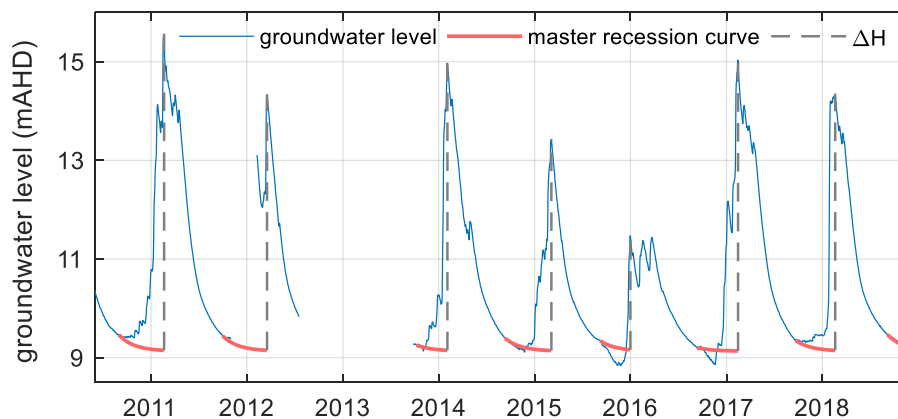
Figure S5. Groundwater level series and master recession curve modelling to calculate annual recharge rates for the shallow aquifer underlying the Howard River catchment. Data from NTG bore RN009421.

Because estimates of Sy for the shallow aquifer are somewhat uncertain (Cook *et al.* 1998), we opted for a water balance approximation to get a more representative estimate of Sy:

$$P = ET + R \quad \xrightarrow{yields} \quad Sy = \frac{P - ET}{\Delta H}$$

With P and ET the measured annual precipitation and evapotranspiration amounts, respectively. Note that we did not include discharge (Q) as an additional output term in this water balance, as we considered that a significant part of Q is already expressed in R. We calculated Sy for the last eight years of data (2011-2018, excluding 2013) and computed the mean of seven Sy estimates (Sy=0.15±0.07).

The last step involved multiplying the annual recharge rate by the mean DIC concentration in the shallow aquifer to obtain an annual rate of DIC export. Here uncertainties were assessed by generating 100,000 sets of DIC concentrations (centred on the median and bounded by two standard deviations of the measured concentrations as per Duvert *et al.* (2020)) and Sy (centred on the mean as obtained above and bounded by two standard deviations), which yielded 100,000 estimates of DIC export for each year. We extracted the median and an error range ($P_{97.5} - P_{2.5}$) from these simulations and for each year. We note that Method 2 also required subtracting our estimate of the downstream (riverine) export of DIC, in order to avoid double accounting.

Method 3. Empirical models

The third method involved calculating CO_2 evasion fluxes by multiplying estimates of the gas transfer velocity (k_{CO2}) to the water–air CO_2 gradient:

$$F_{CO_2} = \sum_t k_{CO2_t} \left(C_{river_t} - C_{atm} \right)$$

Time-dependent estimates of k_{CO2} were obtained by first calculating time-dependent estimates of k_{600} using three empirical models from the literature (Raymond *et al.* 2012):

Model 1: $k_{600_t} = (v_t \times s)^a \times d_t{}^b \times c$

Model 2: $k_{600_t} = e \left(1 - f \times Fr_t{}^2 \right) (v_t \times s)^g \times d_t{}^h$

Model 7: $k_{600_t} = l \, (v_t \times s)^m \times Q_t{}^n \times d_t{}^p$

Where v_t, d_t and Q_t are the river velocity, depth and discharge at bi-hourly timestep t; s is the average river slope (0.00142); Fr is the Froude number at bi-hourly timestep t; a, b and c are the parameters for model 1; e, f, g and h are the parameters for model 2; and l, m, n and p are the parameters for model 7 (Raymond *et al.* 2012). k_{CO2} was then derived from the k_{600} series using the relationship:

$$k_{CO_{2_t}} = k_{600_t} \left(\frac{Sc_{CO2_t}}{600} \right)^{-0.5}$$

Where Sc_{CO2} is a temperature-dependent estimate of the Schmidt number, obtained as per Jähne *et al.* (1987):

$$Sc_{CO_2} = 1923.6 - 125.06 \, T + 4.3773 \, T^2 - 0.085681 \, T^3 + 0.00070284 \, T^4$$

While river discharge and depth were measured, we used hydraulic geometry relationships (Leopold and Maddock 1953) to estimate series of river flow velocity, of use in the models.

Uncertainties were estimated using a Monte Carlo analysis with each model input parameter being randomly selected over their range, as given in Raymond *et al.* (2012). We ran 10,000 simulations for each timestep and extracted an error range ($P_{97.5} - P_{2.5}$). Total annual evasion fluxes were then obtained by summing up the bi-hourly evasion estimates, which yielded 10,000 estimates of total evasion flux, from which we extracted the median. Again, the uncertainty on the total evasion flux according to each model was obtained from the root sum of squared errors on flux estimates at each timestep.

Methods S6. Estimates of NEP

Half-hourly fluxes of heat, moisture and net CO_2 flux were measured for the AU-How and AU-Fog sites. Flux instruments were mounted on guyed masts with adequate homogeneous fetch in all directions and slopes of <1°. According to the eddy-covariance method, the CO_2 flux measured during daytime represents the net exchange of C (NEP) and comprises both uptake via canopy photosynthesis (GPP) and losses from ecosystem respiration (Re). The CO_2 flux measured during night-time is entirely due to Re, and this night-time flux is then extrapolated to daytime periods in order to derive estimates of NEP and GPP fluxes, such as NEP = GPP – Re.

The eddy-covariance flux data were quality-assured and quality-controlled using the OzFlux standard processing protocol implemented through the OzFluxQC v2.9.4 Python scripts, as described by Isaac *et al.* (2017). A number of corrections were applied, including frequency attenuation, 2D coordinate rotation, conversion of sensible heat from virtual to actual flux, application of the WPL correction to account for density effects of heat and water vapour transfer on fluxes, and correction of soil moisture and soil heat flux measurements. This allowed us to obtain level-3 data. Data gaps in the level-3 data were then filled using neural network modelling via the processing package DINGO (Dynamic INtegrated Gap filling and partitioning for OzFlux, Beringer *et al.* 2017), also developed in Python.

From the half-hourly series of GPP, Re and NEP obtained at AU-How, we derived half-hourly, daily, monthly and annual series of NEP across the two years of survey.

Methods S7. Asynchronicity in wetland NEP estimates

The wetland NEP estimates used in this study were not measured at the same time as all other fluxes. We used measurements from Beringer *et al.* (2013) from a seasonal floodplain ~20 km from the Howard River, a dataset that covers three years (2005-2008). To assess how representative of our study period (2016-2018) these earlier wetland measurements were, we compared a number of meteorological and ecosystem variables for those two periods (Table S1).

We found broad similarities in all studied variables between the 2005-2008 and 2016-2018 periods. Rainfall, air temperature and solar radiation were largely similar between the two periods, both during the wet and dry seasons. Likewise, there was no significant difference between the percent area of wetland covered by vegetation in 2005-2008 and in 2016-2018, with similar seasonal dynamics for the two periods. The savanna flux tower (AU-How) has been collecting NEP data since 2001, and fluxes were also comparable between the two study periods.

We used the Kruskal-Wallis test to determine whether wet and dry season datasets were significantly different between the two study periods. For all the variables considered, the null hypothesis could not be rejected (all p-values > 0.14 except for rainfall (0.08); Table S1), pointing to a high degree of similarity between the two periods.

As an additional line of evidence, Beringer *et al.* (2013) found a small range of variation in the annual wetland NEP estimates among the three years of survey (286 to 344 Mg C km^{-2} yr^{-1}; mean 311 Mg C km^{-2} yr^{-1}). Taken together, these analyses indicate that (i) the two periods are indeed comparable in terms of climatic conditions, flooding extent and vegetation growth, and (ii) it is reasonable to assume a relatively low inter-annual variability in wetland NEP.

Table S1. Comparison between meteorological and ecosystem variables at Fogg Dam (i.e. the wetland site studied in Beringer et al., 2013) for the 2005-2008 and 2016-2018 periods. The p-values at the bottom correspond to the null hypothesis that the annual data for the two periods come from the same distribution (Kruskal-Wallis test).

	water year	wet season					dry season				
		P (mm)	T (°C)	vegetation cover (%)	solar radiation (W/m²)	savanna NEP (t/km²)	P (mm)	T (°C)	vegetation cover (%)	solar radiation (W/m²)	savanna NEP (t/km²)
Beringer *et al.* (2013)	2005-2006	1499	27.9	70.2	225.7	277.1	28	23.8	31.7	247.5	155.1
	2006-2007	1722	27.5	72.7	231.7	373.3	33	24.5	43.6	235.8	127.5
	2007-2008	1593	27.8	65.8	235.7	253.2	11	25.5	38.9	241.1	133.7
	mean	**1605**	**27.7**	**69.6**	**231.0**	**301.2**	**24**	**24.6**	**38.1**	**241.5**	**138.8**
this study	2016-2017	1692	27.4	69.8	228.9	380.1	0	25.5	36.0	236.5	144.5
	2017-2018	1674	27.5	65.3	230.8	268.7	4	26.1	43.0	235.7	111.8
	mean	**1683**	**27.4**	**67.5**	**229.8**	**324.4**	**2**	**25.8**	**39.5**	**236.1**	**128.1**
	p-value	0.564	0.139	0.248	0.564	0.564	0.083	0.139	1.000	0.248	0.564

Rainfall and air temperature were obtained from Middle Point BoM station (014041), located < 1 km from Fogg Dam. Solar radiation and savanna NEP were obtained from the Howard Springs eddy-covariance flux tower, located about 20 km from Fogg Dam. Vegetation cover was obtained using quarterly satellite imagery and the VegMachine online tool (https://vegmachine.net/) for the Fogg Dam area.

Methods S8. Fire-related emissions

To estimate fire-related greenhouse gas emissions, we used an Excel spreadsheet version (A. Edwards, personal communication) of the online tool SavBAT 2.2 (https://v2.savbat.environment.gov.au). SavBAT uses vegetation classes and monthly fire scar maps from the North Australia and Rangelands Fire Information service (NAFI). Based on time of year (fire severity), burning efficiency, patchiness, fuel load and emission factors for each grass and woody vegetation class, the algorithm calculates the CO_2, CH_4 and N_2O emissions for a given area (Commonwealth of Australia 2015). Regardless of the vegetation type, both burning efficiency and patchiness factors are higher for late dry season fires, resulting in higher gaseous emissions for these fires. We set the cut-off date from early to late dry season to July 1 instead of August 1 as set in SavBAT by default. This is because the default cut-off date is set for policy reasons in the burning methodology, whereas for the purpose of gaseous emission estimates, fires in July can be considered as late dry season since they are of much higher severity compared to earlier fires (Hutley, Edwards and Setterfield, personal communication).

For the savanna component of the Howard River catchment, vegetation was classified into two types, i.e. 'hOFM' (open forest with mixed grass; ~60% of the catchment area) and 'hWMi' (woodland with mixed grass; ~40%). These two vegetation classes differ in their fuel load accumulation factors as assigned by SavBAT. Fine fuel loads increase with the time since last burn (Table S2), whereas coarser fuel loads are assigned constant values in the model (Table S3).

Table S2. Fine fuel loads for each vegetation class.

years since last burn	fuel load (Mg ha^{-1})	
	hOFM	hWMi
1	2.74	3.8
2	4.25	4.41
3	5.07	4.51
4	5.53	4.53
5	5.78	4.53
>5	6.06	4.53

Table S3. Non-fine fuel loads for each vegetation class.

vegetation class	fuel load (Mg ha^{-1})		
	coarse	heavy	shrub
hOFM	1.4	4.8	1.5
hWMi	0.9	2.2	0.5

For the seasonal wetland component, we assigned the hWMi vegetation type to the whole area. The hWMi class contains more fine fuel load and less coarse fuel load (Tables S2 and S3), which reflects the vegetation assemblage in this landscape component i.e. a mixture of grass-dominated floodplains, flooded woodland and small patches of riparian forest (Figure S6).
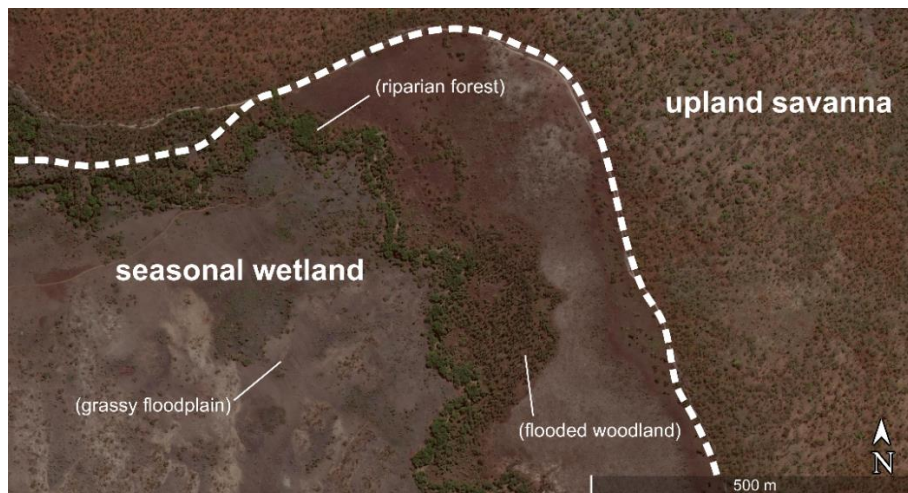
Figure S6. Illustration of the different vegetation assemblages occurring in the wetland landscape component as opposed to upland savanna. The white dashed line represents the boundary between the two landscape components. Image taken from Google Earth (late dry season, September 2017).

Figure S7 shows an example output from SavBAT for a given year. Because outputs using the online tool are given per year only, we used the Excel spreadsheet to derive monthly burnt areas and fire-related CO_2 and CH_4 emissions. We did this for the two years of survey.
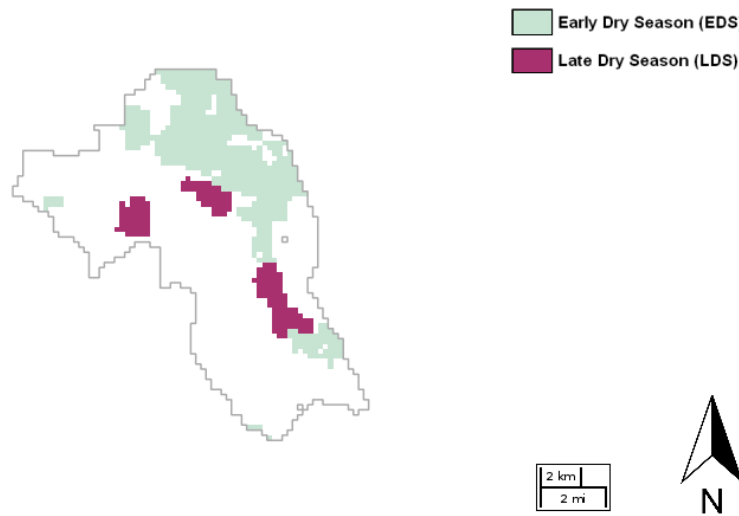
Figure S7. Example of SavBAT output for year 2018. Regardless of the vegetation type, both burning efficiency and patchiness factors are higher for late dry season fires, resulting in higher gaseous emissions for these fires.

Discussion S1. Decoupling between DOC and DIC concentrations
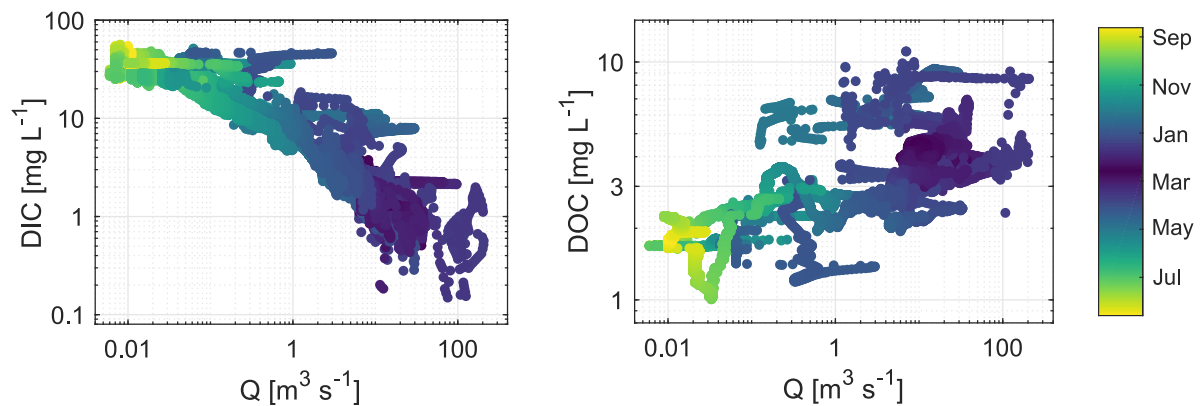
Figure S8. Concentration–discharge relationships in the Howard River for DIC (left) and DOC (right) throughout the two years of survey. Yellow and green colours correspond to data recorded in the dry season, while dark blue colours correspond to the wet season.

DIC concentrations decreased with increasing flow (Figure S8). We explain this dilution pattern (i.e. negative C-Q slope) by the occurrence of a major DIC source in the carbonate aquifer that sustained baseflow during the dry season (Duvert *et al.* 2020). Lower DIC concentrations in the wet season (0.1–5 mg L^{-1}) relative to the dry season (20–60 mg L^{-1}) were likely the result of (i) the dilution of this mineral source by surface waters and shallower flowpaths at high discharge, and (ii) greater CO_2 evasion rates that depleted the riverine DIC pool further. Dilution patterns similar to the one we report here for DIC have been attributed to a decrease in the relative contribution of mineral-rich groundwater at high flow (e.g. Li *et al.* 2017).

In contrast, high DOC concentrations were measured at high discharge (4–11 mg L^{-1}), while baseflow conditions were characterised by lower DOC concentrations (1–3 mg L^{-1}) (Figure S8). This positive C-Q relationship is indicative of a flushing behaviour, likely caused by increased connectivity between organic-rich wetlands, shallow soil and the river during major flow events. This interpretation is consistent with modelling work by Birkel *et al.* (2020), and a common pattern for DOC in streams and rivers (e.g. Boyer *et al.* 1997; Musolff *et al.* 2017; Shih *et al.* 2018; Zhi *et al.* 2019).

The decoupling between DIC and DOC dynamics is not an uncommon observation in the tropics (Shih *et al.* 2018), and can be attributed to changes in water sources across seasons. DOC is mostly associated with organic-rich (shallow) water sources, generally dominant at high flow, whereas DIC typically originates from mineral-rich (deep) groundwater, generally dominant at low flow. Zhi *et al.* (2019) proposed that the alternating dominance of shallow and deeper water sources is the main mechanism leading to contrasting C-Q patterns for different solutes. Our results suggest that the conceptual framework developed by Zhi *et al.* (2019) for temperate catchments also holds for the wet-dry tropics, where flow regimes are governed by shifts in water sources (Birkel *et al.* 2020; Duvert *et al.* 2020).

Despite the dissimilarity in C-Q patterns between DOC and DIC, it is interesting to note that for both C forms the range of variation in concentrations (one and three orders of magnitude for DOC and DIC, respectively) was significantly lower than the range of variation in discharge (four orders of magnitude). This relative chemostatic state reminds us that on an annual scale, both DIC and DOC loads were primarily controlled by discharge (Musolff *et al.* 2017).

References

Beringer J, Livesley SJ, Randle J, Hutley LB (2013) Carbon dioxide fluxes dominate the greenhouse gas exchanges of a seasonal wetland in the wet–dry tropics of northern Australia. *Agricultural and Forest Meteorology* **182-183**, 239-247.

Beringer J, McHugh I, Hutley LB, Isaac P, Kljun N (2017) Technical note: Dynamic INtegrated Gap-filling and partitioning for OzFlux (DINGO). *Biogeosciences* **14**, 1457-1460.

Birkel C, Duvert C, Correa A, Munksgaard NC, Maher DT, Hutley LB (2020) Tracer-aided modelling in the low-relief, wet-dry tropics suggests water ages and DOC export are driven by seasonal wetlands and deep groundwater. *Water Resources Research* **56**, e2019WR026175.

Boix Canadell M, Escoffier N, Ulseth AJ, Lane SN, Battin TJ (2019) Alpine glacier shrinkage drives shift in dissolved organic carbon export from quasi-chemostasis to transport limitation. *Geophysical Research Letters* **46**, 8872-8881.

Boyer EW, Hornberger GM, Bencala KE, McKnight DM (1997) Response characteristics of DOC flushing in an alpine catchment. *Hydrological Processes* **11**, 1635-1647.

Commonwealth of Australia (2015) Carbon Credits (Carbon Farming Initiative—Emissions Abatement through Savanna Fire Management) Methodology Determination 2015. ComLaw, Canberra. http://www.comlaw.gov.au/Details/F2015L00344.

Cook PG, Hatton TJ, Pidsley D, Herczeg AL, Held A, O'Grady A, Eamus D (1998) Water balance of a tropical woodland ecosystem, Northern Australia: A combination of micro-meteorological, soil physical and groundwater chemical approaches. *Journal of Hydrology* **210**, 161-177.

Delin GN, Healy RW, Lorenz DL, Nimmo JR (2007) Comparison of local- to regional-scale estimates of ground-water recharge in Minnesota, USA. *Journal of Hydrology* **334**, 231-249.

Duvert C, Hutley LB, Birkel C, Rudge M, Munksgaard NC, Wynn JG, Setterfield SA, Cendón DI, Bird MI (2020) Seasonal shift from biogenic to geogenic fluvial carbon caused by changing water sources in the wet-dry tropics. *Journal of Geophysical Research: Biogeosciences* **125**, e2019JG005384.

Harned HS, Davis R (1943) The ionization constant of carbonic acid in water and the solubility of carbon dioxide in water and aqueous salt solutions from 0 to 50°. *Journal of the American Chemical Society* **65**, 2030-2037.

Healy RW, Cook PG (2002) Using groundwater levels to estimate recharge. *Hydrogeology Journal* **10**, 91-109.

Horgby Å, Segatto PL, Bertuzzo E, Lauerwald R, Lehner B, Ulseth AJ, Vennemann TW, Battin TJ (2019) Unexpected large evasion fluxes of carbon dioxide from turbulent streams draining the world's mountains. *Nature Communications* **10**, 4888.

Hutchins RHS, Tank SE, Olefeldt D, Quinton WL, Spence C, Dion N, Estop-Aragonés C, Mengistu SG (2020) Fluvial CO_2 and CH_4 patterns across wildfire-disturbed ecozones of subarctic Canada: Current status and implications for future change. *Global Change Biology* **26**, 2304-2319.

Isaac P, Cleverly J, McHugh I, van Gorsel E, Ewenz C, Beringer J (2017) OzFlux data: network integration from collection to curation. *Biogeosciences* **14**, 2903-2928.

Jähne B, Heinz G, Dietrich W (1987) Measurement of the diffusion coefficients of sparingly soluble gases in water. *Journal of Geophysical Research: Oceans* **92**, 10767-10776.

Langergraber G, Fleischmann N, Hofstädter F (2003) A multivariate calibration procedure for UV/VIS spectrometric quantification of organic matter and nitrate in wastewater. *Water Science and Technology* **47**, 63-71.

Leopold LB, Maddock TJ (1953) 'The hydraulic geometry of stream channels and some physiographic implications.' 252, Washington, D.C.

Li L, Bao C, Sullivan PL, Brantley S, Shi Y, Duffy C (2017) Understanding watershed hydrogeochemistry: 2. Synchronized hydrological and geochemical processes drive stream chemostatic behavior. *Water Resources Research* **53**, 2346-2367.

Maher DT, Santos IR, Golsby-Smith L, Gleeson J, Eyre BD (2013) Groundwater-derived dissolved inorganic and organic carbon exports from a mangrove tidal creek: The missing mangrove carbon sink? *Limnology and Oceanography* **58**, 475-488.

Musolff A, Fleckenstein JH, Rao PSC, Jawitz JW (2017) Emergent archetype patterns of coupled hydrologic and biogeochemical responses in catchments. *Geophysical Research Letters* **44**, 4143-4151.

Plummer LN, Busenberg E (1982) The solubilities of calcite, aragonite and vaterite in CO_2-H_2O solutions between 0 and 90°C, and an evaluation of the aqueous model for the system $CaCO_3$-CO_2-H_2O. *Geochimica et Cosmochimica Acta* **46**, 1011-1040.

Raymond PA, Zappa CJ, Butman D, Bott TL, Potter J, Mulholland P, Laursen AE, McDowell WH, Newbold D (2012) Scaling the gas transfer velocity and hydraulic geometry in streams and small rivers. *Limnology and Oceanography: Fluids and Environments* **2**, 41-53.

Runkel RL, Crawford CG, Cohn TA (2004) 'Load estimator (LOADEST): a FORTRAN program for estimating constituent loads in streams and rivers.' 4-A5.

Saraceno JF, Shanley JB, Downing BD, Pellerin BA (2017) Clearing the waters: Evaluating the need for site-specific field fluorescence corrections based on turbidity measurements. *Limnology and Oceanography: Methods* **15**, 408-416.

Shih YT, Chen PH, Lee LC, Liao CS, Jien SH, Shiah FK, Lee TY, Hein T, Zehetner F, Chang CT, Huang JC (2018) Dynamic responses of DOC and DIC transport to different flow regimes in a subtropical small mountainous river. *Hydrology and Earth System Sciences* **22**, 6579-6590.

Zhi W, Li L, Dong W, Brown W, Kaye J, Steefel C, Williams KH (2019) Distinct source water chemistry shapes contrasting concentration-discharge patterns. *Water Resources Research* **55**, 4233-4251.